Visible Light-Induced Water Oxidation on Mesoscopic α-Fe₂O₃ Films Made by Ultrasonic Spray Pyrolysis

Alexis Duret and Michael Grätzel*

Laboratory of Photonics and Interfaces (LPI), Swiss Federal Institute of Technology, CH-1015 Lausanne, Switzerland

α-Fe₂O₃ films having a mesoscopic leaflet type structure were produced for the first time by ultrasonic spray pyrolysis (USP) to explore their potential as oxygen-evolving photoanodes. The target of these studies is to use translucent hematite films deposited on conducting fluorine doped tin oxide (FTO) glass as top electrodes in a tandem cell that accomplishes the cleavage of water into hydrogen and oxygen by sunlight. The properties of layers made by USP were compared to those deposited by conventional spray pyrolysis (SP). Although both types of films show similar XRD and UV−visible and Raman spectra, they differ greatly in their morphology. The mesoscopic α-Fe₂O₃ layers produced by USP consist mainly of 100 nm-sized platelets with a thickness of 5−10 nm. These nanosheets are oriented mainly perpendicularly to the FTO support, their flat surface exposing (001) facets. The mesoscopic leaflet structure has the advantage that it allows for efficient harvesting of visible light, while offering at the same time the very short distance required for the photogenerated holes to reach the electrolyte interface before recombining with conduction band electrons. This allows for water oxidation by the valence band holes even though their diffusion length is only a few nanometers. Distances are longer in the particles produced by SP favoring recombination of photoinduced charge carriers. Open-circuit photovoltage measurements indicate a lower surface state density for the nanoplatelets as compared to the round particles. These factors explain the much higher photoactivity of the USP compared to the SP deposited α-Fe₂O₃ layers. Addition of hydrogen peroxide to the alkaline electrolyte further improves the photocurrent−voltage characteristics of films generated by USP indicating the hole transfer from the valence band of the semiconductor oxide to the adsorbed water to be the rate-limiting kinetic step in the oxygen generation reaction.

1. Introduction

The visible light-induced cleavage of water into hydrogen and oxygen remains the main target of current photoelectrochemical research.[1−5] Several configurations are presently explored to achieve this challenging task. For example, a photoelectrode can be coupled with a dark counter electrode or with a photoactive cathode. Alternatively, two photoelectrodes of a different band gap can be superimposed and coupled with a dark counter electrode. The last embodiment, called "tandem cell",[6] is the most attractive configuration from the perspective of solar to chemical conversion efficiency.[7]

For optimal performance, the two superimposed photosystems should absorb complementary parts of the visible and near-infrared range of the solar emission spectrum. Tungsten trioxide and hematite (α-Fe₂O₃) are suitable semiconductor oxides to serve as oxygen-evolving anodes absorbing photons from the blue and ultraviolet parts of the solar emission because of their band gaps of 2.2 and 2.6 eV, respectively. α-Fe₂O₃, in particular, is inexpensive and stable under operation resisting both dark and photocorrosion.[8] However, despite significant research effort over recent decades,[8−17] the photocurrents obtained from α-Fe₂O₃ thin film anodes in air-mass 1.5 sunlight have remained low, that is, less than 1 mA/cm² for a single hematite layer at a bias voltage of 1.2 V against the reversible hydrogen electrode (RHE). Under similar conditions, WO₃ yields photocurrents of 2.5 mA/cm² despite its larger band gap.[2,18,19] The poor photoelectrochemical performance of α-Fe₂O₃ has been attributed to
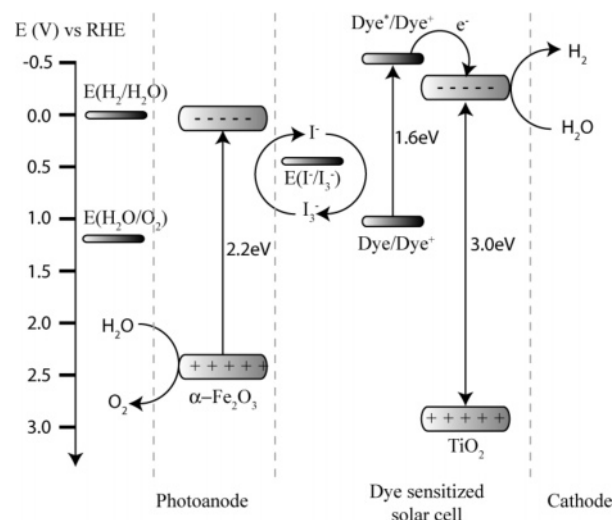

Figure 1. Band diagram of the tandem cell.

the short charge carrier diffusion lengths[20] and to the slow kinetics of water oxidation by the valence band holes.[9]

The goal of our investigation is to use the translucent hematite film as a top electrode in a tandem cell affording water cleavage by visible light. A schematic energy level diagram of the device is shown in Figure 1. When sunlight strikes the cell, the top electrode will absorb the green, blue, and ultraviolet photons
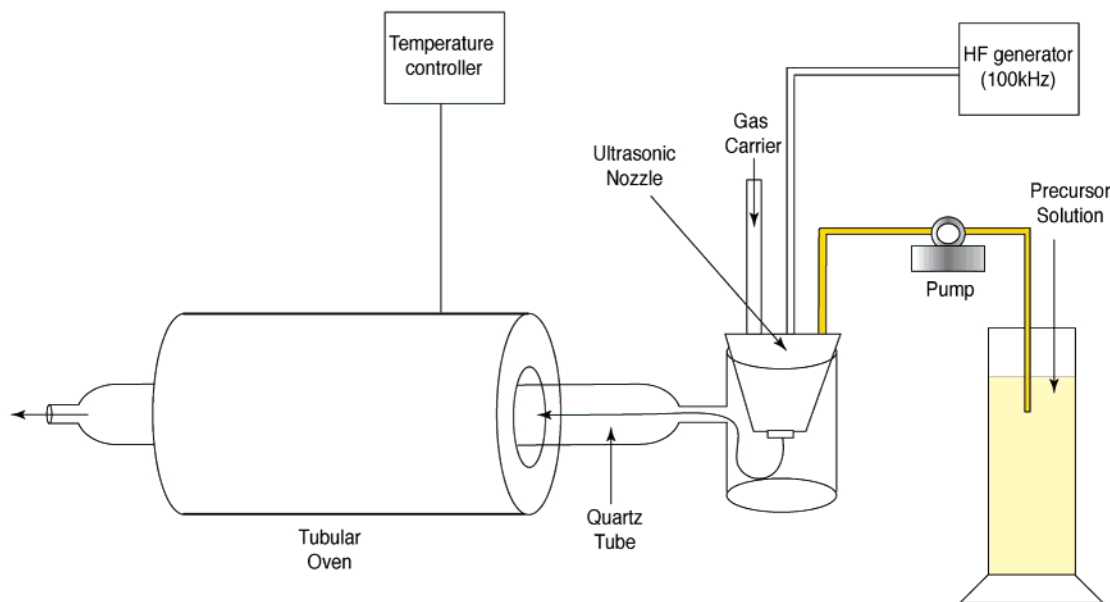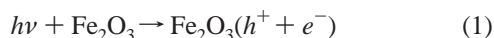
Visible Light-Induced Water Oxidation

J. Phys. Chem. B, Vol. 109, No. 36, 2005 **17185**

Figure 2. Schematic drawing of the ultrasonic spray set up.

having a wavelength below 600 nm. The photoexcitation produces electron−hole pairs in the iron oxide film

$$hv + Fe_2O_3 \rightarrow Fe_2O_3(h^+ + e^-) \qquad (1)$$

The holes migrate in the valence band to the surface where they react with water producing oxygen and protons.

$$4h^+ + 2H_2O \rightarrow 4H^+ + O_2 \qquad (2)$$
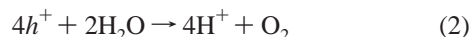
The photogenerated electrons travel in the conduction band of the iron oxide to the conducting glass support serving as a current collector. From there, they are injected into the cathode of the bottom cell, for example, a dye-sensitized solar cell. The latter absorbs the light in the red and near-infrared spectral region, which is transmitted by the iron oxide. The photocurrent generated in the bottom cell by the transmitted light must at least be as high as the current produced in the top electrode. By passing through the bottom cell, the electrochemical potential of the electrons is increased permitting reduction of water to hydrogen.

$$2e^- + 2H^+ \rightarrow H_2 \qquad (3)$$

The present work reports for the first time on an ultrasonic spray pyrolysis procedure to produce α-Fe₂O₃ (hematite) films with a leaflet type mesoscopic structure, whose photoactivity was found to be superior to that of hematite layers deposited by conventional spray pyrolysis.

2. Experimental Section

2.1. Film Synthesis. Two deposition methods were used to deposit semitransparent thin films of hematite onto the transparent conducting glass (TCO) substrate (Tek15, Hartford Glass Co., 15 Ω/sq).

(a) Spray Pyrolysis (SP). Twenty milliliters of a 0.05 M solution of ferric acetylacetonate (Fluka) in ethanol (absolute, purum from Fluka) was sprayed onto the TCO substrate maintained at 400 °C. This setup was designed such that the spraying process occurred only when the substrate temperature was above 400 °C (pulsed deposition). The carrier gas was nitrogen at 1 bar.

(b) Ultrasonic Spray Pyrolysis (USP). A schematic drawing of the USP setup is shown in Figure 2. It is similar to the one used by Wang et al.:[21] 0.02 M of ferric acetylacetonate (Fluka) dissolved in ethanol (absolute, purum from Fluka) was first pumped to the ultrasonic nozzle (US-1, Lechler) at a flow rate of 1 mL/min. This nozzle was connected to a 100 kHz frequency generator. The droplets of precursor solution generated are then injected into a glass chamber used to prevent big droplets from entering the tubular oven. The fog of small droplets obtained at the outlet of this chamber is finally carried in a tubular oven heated at 420 °C (temperature of the substrate under steady-state conditions) using compressed air (8 bar) at a flow rate of 20 L/min. The optimal sprayed volume of precursor solution was 200 mL and the distance between the substrate and the outlet of the chamber was 25 cm.

2.2. Spectroscopic and Photoelectrochemical Characterization. Films were characterized by UV−vis spectroscopy using a Hewlett-Packard 8453 UV−visible spectrophotometer. The morphology was examined using a Philips XL 30 FEG scanning electron microscope. The thickness of the samples was measured using an alpha-step (Tencor Alpha-Step 500) profilometer. The crystalline phases were identified with a Siemens powder X-ray diffractometer using Cu Kα radiation. The Raman spectra of the different samples were measured using a Renishaw RM2000 Raman microscope at room temperature at a wavelength of 514.5 nm and at an intensity of 0.9 mW (spot size: 2−3 μm in diameter).

The photoelectrochemical measurements were carried out in a standard three-electrode cell using a Ag/AgCl reference electrode and a platinum foil as counter electrode (5 cm²). All the potentials reported here are given against the reversible hydrogen electrode (RHE) except as otherwise stated. The photocurrents measured under white light were obtained using a 450W Xe lamp; the UV and IR part were cut off using a KG3 filter from Schott and the light intensity was adjusted to simulate global air mass 1.5 solar radiation using neutral density filters. The spectral mismatch factor was estimated to be 1.3 corresponding to an equivalent solar intensity of ca. 130 mW/cm². The incident photon to current conversion efficiency (IPCE) was measured as a function of the excitation wavelength using a 450 W Xe lamp coupled to a Bausch&Lomb monochromator with a bandwidth of 5 nm. A solution of 1 M NaOH
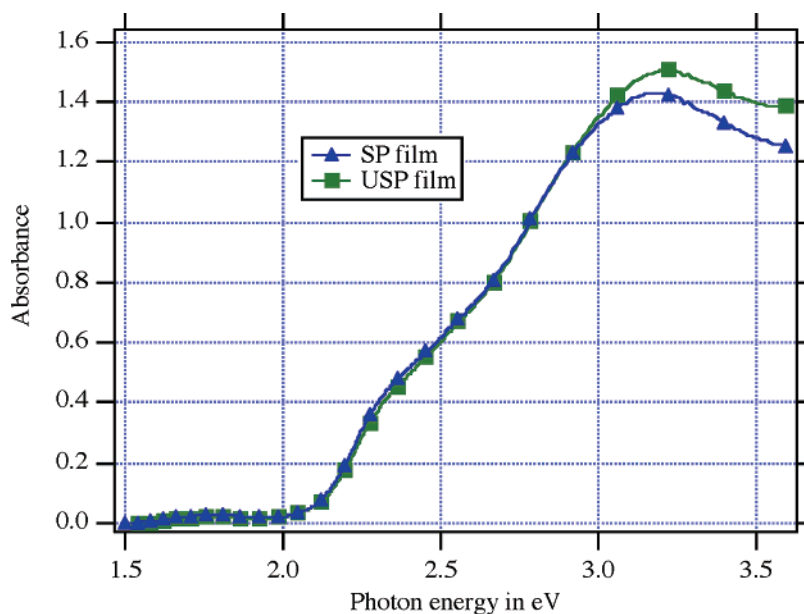
Figure 3. Absorption spectra of USP (TA6) and SP (S13) sample.

(extra pure, Fluka) was used for all the electrochemical measurement.

Open-circuit photopotentials were measured using the following procedure: first, the redox potential of the redox solutions used was measured with a platinum foil electrode against a Ag/AgCl reference electrode; then, the potential between the photoanode and the platinum electrode was measured in the same solution in the dark and under AM1.5. The open-circuit photopotential was considered to be the potential under AM1.5 minus the dark potential. This procedure is similar to the one described by Sanchez.[22]

3. Results and Discussion

3.1. Optical Characterization. The films obtained by both methods are red-brown and semitransparent. Their thickness measured by the alpha step apparatus is around 200 nm. Their absorption is very similar over the whole visible spectrum, the onset being around 620 nm in accordance with the band gap of α-Fe_2O_3 (Figure 3). Using eq 4,[23] it is possible to estimate the nature and onset of the electronic transitions:

$$(\alpha h\nu) = A_o(h\nu - E_g)^m \tag{4}$$

where α is the absorption coefficient, $h\nu$ is the photon energy in eV, and E_g is the band gap energy in eV. A_o and m are constants, which depend on the kind of electronic transition, m being equal to $1/2$ for a direct allowed and 2 for an indirect forbidden transition.

Shown in Figure 4a and b are plots of the absorption data according to eq 4. Both samples exhibit an indirect transition at 2 eV and direct transition at 3.1 and 3.2 eV for the SP and USP layers, respectively. Similar values have already been reported in the literature.[24–27] The indirect transition has been identified as a spin-forbidden Fe^{3+} 3d→3d excitation while the direct transition corresponds to the O^{2-} 2p→Fe^{3+} 3d charge transfer.

3.2. Morphology. Figure 5 shows SEM pictures of the two samples. The two deposition methods give films with very different morphologies. The SP sample is made of spherical particle with a diameter between 50 and 150 nm and a wide size distribution. Such a structure is typically obtained by rapid

deposition using spray pyrolysis.[14,28] The USP sample features mesoscopic leaflets having a thickness of 5–10 nm and a length between 50 and 100 nm. From previous studies of hematite colloids,[29–32] one infers the flat surface of the platelets to have (001) orientation, their edge exposing (012) planes.[30] This morphology reflects the slow growth rate (ca. 1 nm/min) of the sample deposited by USP. Indeed, USP resembles the atmospheric chemical vapor deposition method in that the precursor is vaporized and partly decomposed before it is deposited onto the substrate.

3.3. XRD Spectroscopy. The XRD spectra of USP and SP samples are presented in Figure 6. Since the photoelectrochemical performance of the α-Fe_2O_3 is strongly dependent on the substrate on which it has been deposited, XRD spectra were measured using TCO as substrate. Therefore, the main peaks of these spectra arise from the fluorine-doped SnO_2 underlayer. Nevertheless, some peaks characteristic of iron oxides can be distinguished. Both samples exhibit features characteristic of the α-Fe_2O_3 crystallographic phase. Apparently, both samples also contain some amount of magnetite (Fe_3O_4); the film made by USP seems to be richer in Fe_3O_4 than the one made by SP. It has already been reported in the literature[14,33] that thin films of α-Fe_2O_3 may contain Fe_3O_4 or maghemite (γ-Fe_2O_3).

3.4. Raman Spectroscopy. Raman spectroscopy is often used in the analysis of the corrosion products of iron[34] as it allows distinguishing readily between the different crystallographic phases of iron oxides. It can also be used to establish the preferential crystallographic orientation of a sample.[35] Figure 7 presents the Raman spectra of both samples. As shown in Table 1, the main peaks of these spectra can be assigned to the α-Fe_2O_3 crystallographic phase.[14,36] The peak at 656 cm^{-1} corresponds to an impurity phase; it may be Fe_3O_4, FeO, or γ-Fe_2O_3 since all three compounds exhibit a peak[36] around 660 cm^{-1}. However, γ-Fe_2O_3 has a doublet at 667 and 718 cm^{-1}. Moreover, as stated by Jorand Sartoretti et al.,[14] FeO and γ-Fe_2O_3 are not stable at room temperature;[37] therefore, they are very unlikely to be present in the samples. Hence, the peak at 656 cm^{-1} is probably due to Fe_3O_4. The relative intensity of the impurity peak compared to the α-Fe_2O_3 peaks is higher in the USP than in the SP sample, implying that the USP sample

Visible Light-Induced Water Oxidation

J. Phys. Chem. B, Vol. 109, No. 36, 2005 **17187**
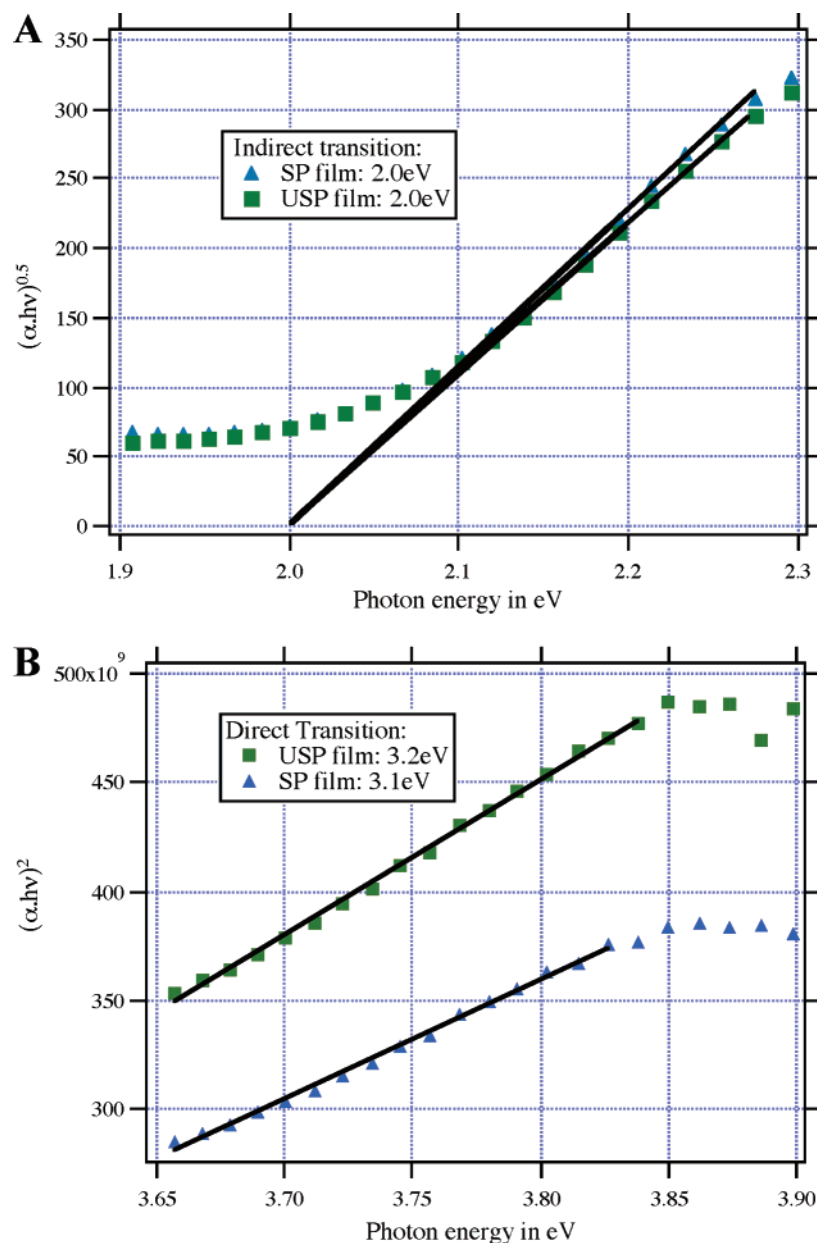

Figure 4. (A) Calculation of the indirect and (B) the direct electronic transition.
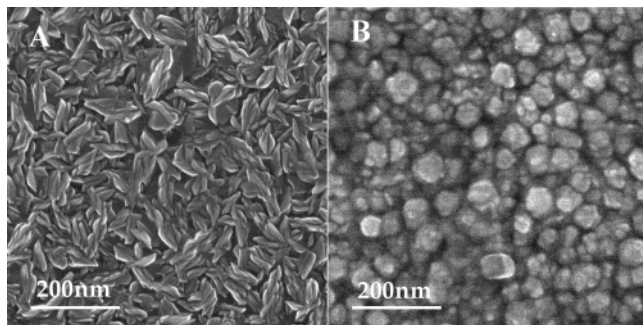

Figure 5. SEM picture (top view) of the (A) USP and (B) SP sample.

contains a higher concentration of Fe_3O_4 than the SP sample. This confirms the results of the XRD analysis.

3.5. Electrochemical and Photoelectrochemical Measurements. Current−potential curves have been measured in the dark and under AM1.5 simulated sunlight for both samples in 1 M NaOH. Figure 8 shows that the two films behave very differently. The dark current of the USP sample rises gradually at potentials greater than 1.2 V versus RHE to reach 0.15 mA/cm^2 at 1.6 V, whereas the dark current of the SP sample increases more steeply to reach 0.25 mA/cm^2 at 1.6 V. The photocurrent onset potential is at 550 and 1125 mV versus RHE for the USP and the SP sample, respectively. Apparently, a higher applied potential is needed to afford water oxidation for the SP sample than for the USP sample. These onset potentials are several hundred millivolts more positive than the flat band potential of hematite.[38] This may be explained by the presence of a deep interband donor state as shown by Horowitz.[39] The photocurrent reaches 1.07 mA/cm^2 and 14 μA/cm^2 at 1200 mV versus RHE for the USP and the SP sample, respectively. It does not reach a plateau even at higher potentials for both samples. The current potential was measured several times without noticeable change.

The effect of hydrogen peroxide addition on the photoelectrochemical behavior of the α-Fe_2O_3 was also measured. The goal of this test was to check whether the photocurrent and the onset potential are affected by a species easier to oxidize than hydroxide. Figure 9 compares the photocurrent measured using
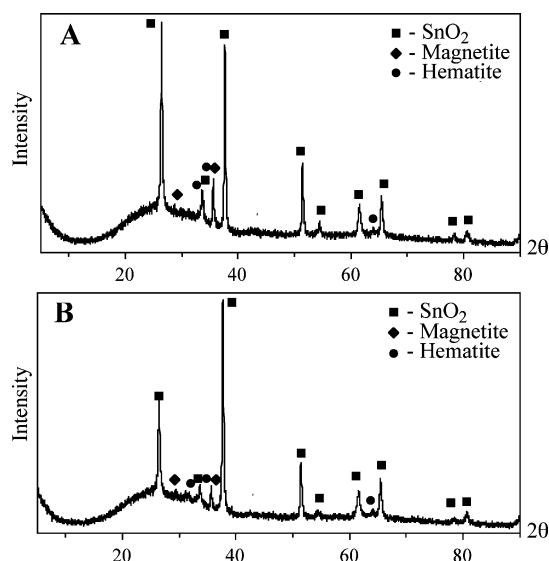
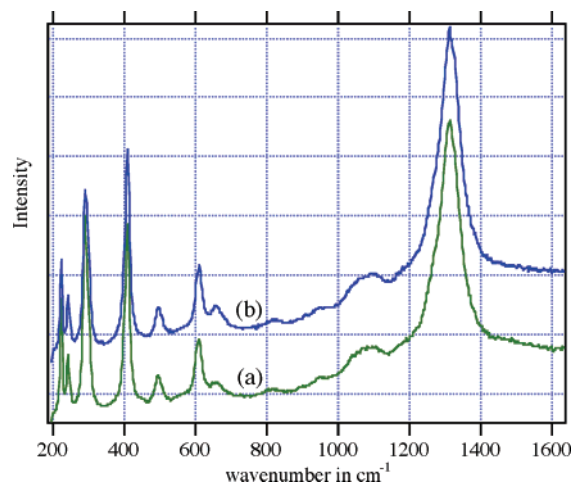**Figure 6.** XRD spectrum of film prepared by (A) USP and (B) SP.

Figure 7. Raman spectra of films prepared by (a) SP and (b) USP.

TABLE 1: Identification of the Main Peaks of the Raman Spectra

peaks in cm^{-1}	crystallographic phase
224	α-Fe$_2$O$_3$
244	α-Fe$_2$O$_3$
292	α-Fe$_2$O$_3$
409	α-Fe$_2$O$_3$
656	Fe$_3$O$_4$
612	α-Fe$_2$O$_3$
499	α-Fe$_2$O$_3$
1315	α-Fe$_2$O$_3$

both SP and USP electrodes in NaOH 1 M and in NaOH 1 M + H$_2$O$_2$ 0.5 M. The addition of H$_2$O$_2$ in the electrolyte enhances greatly the photocurrent for both samples and lowers the onset potential by 600 mV and 200 mV for the SP and USP sample, respectively. Itoh and Bockris[40] have reported a similar effect on hematite thin film electrodes and explained it by the fact that α-Fe$_2$O$_3$ valence band holes oxidize H$_2$O$_2$ 10 times faster than H$_2$O. Current doubling may also contribute to the increase in the photocurrent, since H$_2$O$_2$ is known to induce such effects.[41,42]

3.6. IPCE Curves. The IPCE curves of the two samples at different potentials are given in Figure 10; they have been measured at 1200, 1400, and 1600 mV versus RHE for the USP and only at 1600 mV for the SP sample (because of very low photocurrent under monochromatic light at lower potentials).
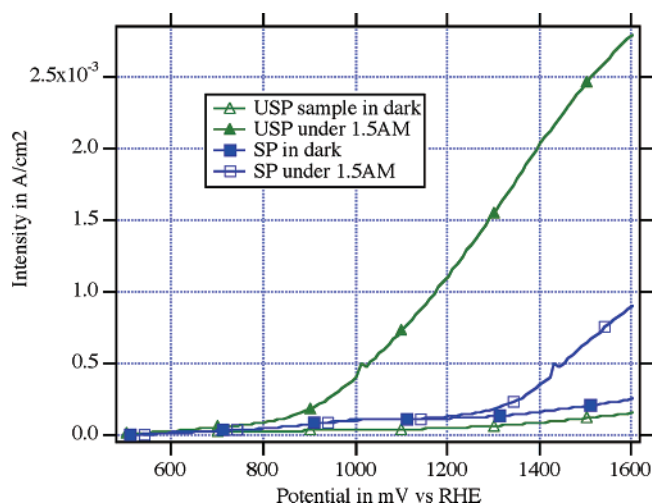

Figure 8. Current potential curves for the SP and USP sample measured in NaOH 1 M in the dark and under simulated air mass 1.5 sunlight (equivalent intensity 130 mW/cm^2) at a scan rate of 100 mV/s.

The IPCE curves all have a maximum value at 370 nm, corresponding to the maximum of the optical absorption. As expected, the IPCE of the SP sample is much lower than the IPCE of the USP sample. The IPCE curves have a similar shape: their onset is around 600 nm, augmenting toward shorter wavelengths. For the USP electrode, at 1.6 V the IPCE quadruples from 6% to 24% by decreasing the wavelength from 500 to 400 nm while the absorption of the films increases by a much smaller increment, that is, from 70 to 96%. Because each absorbed photon produces an electron−hole pair in the Fe$_2$O$_3$ film, the incident photon to current conversion efficiency is the product of the cross section for light absorption and carrier collection:

$$\text{IPCE} = \eta_{\text{abs}}\eta_{\text{coll}} \tag{5}$$

Thus, it appears that the carrier collection cross section augments with increasing energy of the photons. Further studies are required to examine the reasons for this interesting behavior.

IPCE spectra normalized at 370 nm are shown in Figure 11 for different applied potentials. There is an increase in the visible part of the normalized IPCE spectra with applied potential for the USP sample. It is clear that green photons are absorbed closer to the SnO$_2$/Fe$_2$O$_3$ than the blue or ultraviolet ones. This would imply that the region of the film close to the interface is less photoactive than the protruding nanoleaflets. Further studies including the examination of any role of light scattering are being performed presently to substantiate this phenomenon. The normalized IPCE spectrum of the SP sample at 1.6 V overlaps with the spectra of the USP sample measured at 1.2 and 1.4 V versus RHE.

3.7. Photopotential Measurements. Figure 12 shows the photopotential measured under AM 1.5 sunlight in the presence of different redox couples as a function of their Nernst potential. Details are listed in Table 2. For an ideal semiconductor−electrolyte Schottky junction, the photopotential should follow eq 6:[43]

$$V_{\text{OC}} = V_{\text{FB}} - V_{\text{redox}} \tag{6}$$

where V_{OC} is the open-circuit photopotential, V_{FB} is the flat band potential, and V_{redox} is the redox potential of the redox couple present in the electrolyte in contact with the photoelectrode. The slope of the photopotential versus the redox potential
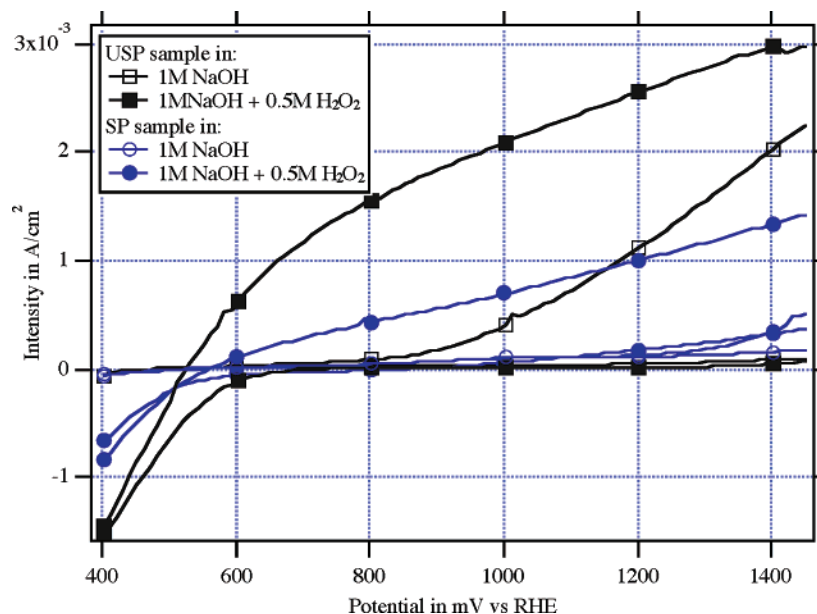
Visible Light-Induced Water Oxidation

J. Phys. Chem. B, Vol. 109, No. 36, 2005 **17189**

Figure 9. Current potential curves for SP and USP sample measured in NaOH 1 M and in the absence and presence of 0.5 M H_2O_2 under simulated solar light at a scan rate of 100 mV/s.
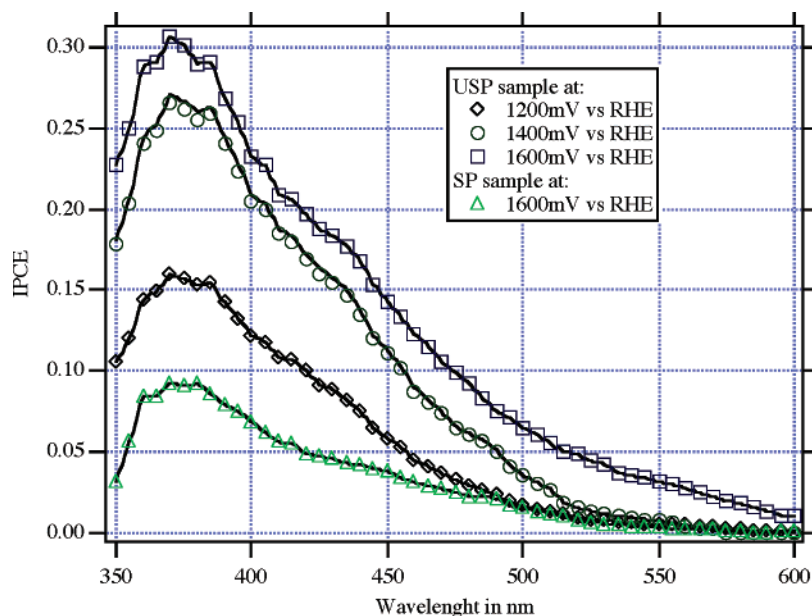

Figure 10. IPCE of the USP and SP samples measured at different potentials in 1 M NaOH.

TABLE 2: Redox Couples, Corresponding Redox Potential, and Photopotential Measured for Both Samples

	SP		USP
redox couple	V_{rdx} [V] vs Ag/AgCl	V_{OC} [V]	V_{OC} [V]
Br^-/BrO_3^-	−0.10	0.14	0.03
OH^-/O_2	−0.04	0.22	0.06
$Fe(CN)_6^{3-}/Fe(CN)_6^{3-}$	0.11	0.31	0.19
$Fe(CN)_6^{3-}/Fe(CN)_6^{3-}$	0.21	0.31	0.31
$Fe(CN)_6^{3-}/Fe(CN)_6^{3-}$	0.22	0.35	0.33

approaches 1 for the USP sample indicating an ideal behavior as predicted by eq 6. This is similar to the observation by Sanchez et al.[22] with a Nb doped α-Fe₂O₃ single crystal. The intercept of the USP photopotential curve is at ∼∠0.1 V versus Ag/AgCl; this value is more positive than the flat band potential reported in the literature in similar conditions. The difference is ascribed to the insufficient light intensity used during our photopotential measurements[44] and a positive shift of the flat

band potential under illumination because of the accumulation of valence band holes at the surface.[45] For the SP sample, the slope is ∼0.5. This suggests that the Fermi level of the electrode is partially pinned, a change of 0.1 V in the redox potential inducing a change of 0.05 V in the photopotential. A similar behavior has already been reported for polycrystalline α-Fe₂O₃ samples.[46] The dark potential for the USP sample was close to 0 V for all redox couples. However, the dark potential was negative and dependent on the redox couple for the SP sample. This may be due to charging of surface states via electron-transfer reactions with the redox couple in solution.[46] These results show that the surface state concentration is smaller for the USP ($<10^{12}$ cm^{-2})[43] than for the SP sample where the charge due to surface states is of the same order of magnitude as the charge due to the space charge layer.[43] It shows also that surface state concentration in the SP sample is important enough to induce a partial Fermi level pinning. These results corroborate the statements made by Sanchez et al.[22] and Shinar et al.:[46] the
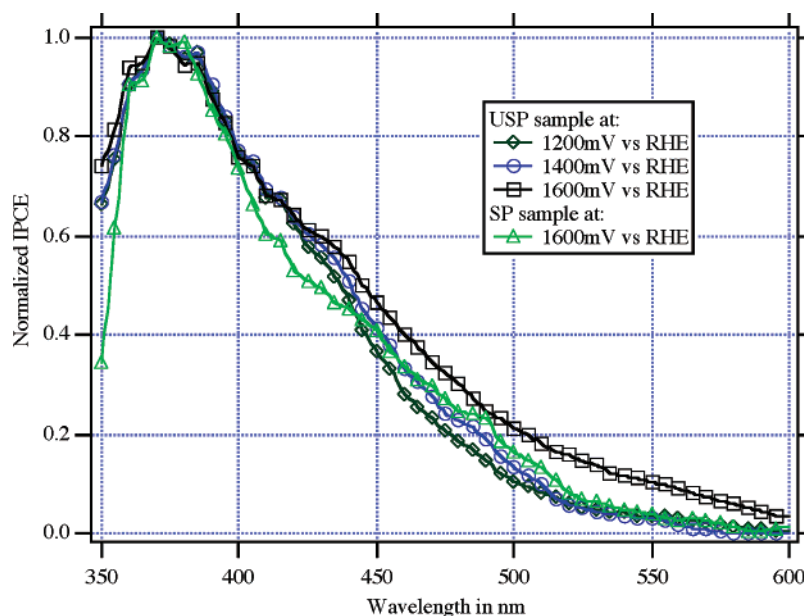
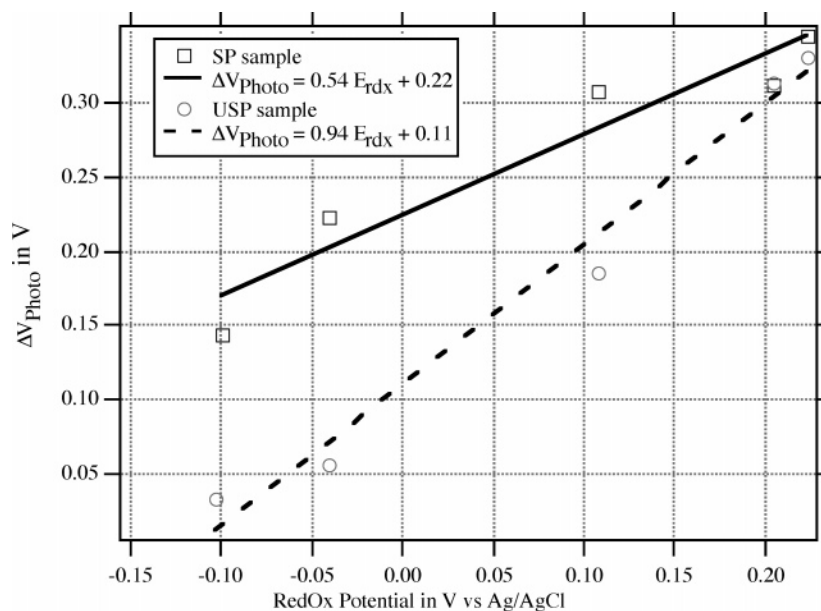**Figure 11.** IPCE normalized at 370 nm of the USP and SP samples measured at different potentials in 1 M NaOH.

Figure 12. Open-circuit photovoltage under 1.5AM vs redox potential.

surface quality of α-Fe_2O_3 photoanode is strongly dependent on the preparation conditions.

4. Conclusions

The deposition of 200-nm α-Fe_2O_3 thin films by SP and USP has been described. Optical studies have shown that these two samples have one indirect (2.0 eV) and one direct (3.0 eV) electronic transition. It has also been shown by XRD and Raman spectroscopy that the two samples contained mainly the α-Fe_2O_3 phase and at least one impurity phase (Fe_3O_4). Apparently, the concentration of Fe_3O_4 is more important in the USP sample than in the SP sample. Although the films show similar XRD and UV–visible and Raman spectra, they differ greatly in their morphology. The mesoscopic α-Fe_2O_3 layers produced by USP consist mainly of 100-nm-sized platelets with a thickness of 5–10 nanometers. These nanosheets are oriented perpendicularly to the FTO support, their flat surface exposing (001) facets. The mesoscopic leaflet structure has the advantage that it allows for efficient harvesting of visible light, while offering at the same time the very short distance required for the photogenerated holes to reach the electrolyte interface before recombining with conduction band electrons. This allows for water oxidation by the valence band holes even though their diffusion length is only a few nanometers. Distances are longer in the particles produced by SP favoring recombination of photoinduced charge carriers. Open-circuit photovoltage measurements indicate a lower surface state density for the nanoplatelets as compared to the round particles. These factors explain the much higher photoactivity of the USP compared to the SP deposited α-Fe_2O_3 layers. Further development of these promising hematite photoanaodes having a mesoscopic platelet structure is being pursued in our laboratory.

Visible Light-Induced Water Oxidation

J. Phys. Chem. B, Vol. 109, No. 36, 2005 **17191**

References and Notes

(1) Majumder, S. A.; Khan, S. U. M. *Int. J. Hydrogen Energy* **1994**, *19*, 881.

(2) Santato, C.; Ulmann, M.; Augustynski, J. *Adv. Mater.* **2001**, *13*, 511.

(3) Akikusa, J.; Khan, S. U. M. *Int. J. Hydrogen Energy* **2002**, *27*, 863.

(4) Lindgren, T.; Wang, H. L.; Beermann, N.; Vayssieres, L.; Hagfeldt, A.; Lindquist, S. E. *Sol. Energy Mater. Sol. Cells* **2002**, *71*, 231.

(5) Ingler, W. B.; Khan, S. U. M. *Abstr. Pap.—Am. Chem. Soc.* **2003**, *225*, U508.

(6) Fan, J. C. C.; Tsaur, B. Y.; Palm, B. J. *Proc. Soc. Photo-Opt. Instrum. Eng.* **1983**, *407*, 73.

(7) Weber, M. F.; Dignam, M. J. *J. Electrochem. Soc.* **1984**, *131*, 1258.

(8) Kennedy, J. H.; Anderman, M. *J. Electrochem. Soc.* **1983**, *130*, 848.

(9) Dareedwards, M. P.; Goodenough, J. B.; Hamnett, A.; Trevellick, P. R. *J. Chem. Soc., Faraday Trans. 1* **1983**, *79*, 2027.

(10) Kennedy, J. H.; Frese, K. W. *J. Electrochem. Soc.* **1977**, *124*, C130.

(11) Kennedy, J. H.; Shinar, R.; Ziegler, J. P. *J. Electrochem. Soc.* **1980**, *127*, 2307.

(12) Quinn, R. K.; Nasby, R. D.; Baughman, R. J. *Mater. Res. Bull.* **1976**, *11*, 1011.

(13) Antonucci, V.; Passalacqua, E.; Giordano, N. *Ber. Bunsen-Ges. Phys. Chem.* **1986**, *90*, 828.

(14) Sartoretti, C. J.; Ulmann, M.; Alexander, B. D.; Augustynski, J.; Weidenkaff, A. *Chem. Phys. Lett.* **2003**, *376*, 194.

(15) Khan, S. U. M.; Akikusa, J. *J. Phys. Chem. B* **1999**, *103*, 7184.

(16) Beermann, N.; Vayssieres, L.; Lindquist, S. E.; Hagfeldt, A. *J. Electrochem. Soc.* **2000**, *147*, 2456.

(17) Bjorksten, U.; Moser, J.; Gratzel, M. *Chem. Mater.* **1994**, *6*, 858.

(18) Santato, C.; Odziemkowski, M.; Ulmann, M.; Augustynski, J. *J. Am. Chem. Soc.* **2001**, *123*, 10639.

(19) Santato, C.; Ulmann, M.; Augustynski, J. *J. Phys. Chem. B* **2001**, *105*, 936.

(20) Kennedy, J. H.; Frese, K. W. *J. Electrochem. Soc.* **1978**, *125*, 709.

(21) Wang, S. Y.; Wang, W.; Wang, W. Z.; Jiao, Z.; Liu, J. H.; Qian, Y. T. *Sens. Actuators, B* **2000**, *69*, 22.

(22) Sanchez, C.; Sieber, K. D.; Somorjai, G. A. *J. Electroanal. Chem.* **1988**, *252*, 269.

(23) Pankov, J. I. *Optical processes in semiconductors*; Prentice Hall: New Jersey, 1971.

(24) Marusak, L. A.; Messier, R.; White, W. B. *J. Phys. Chem. Solids* **1980**, *41*, 981.

(25) Tandon, S. P.; Gupta, J. P. *Spectrosc. Lett.* **1970**, *3*, 297.

(26) Debnath, N. C.; Anderson, A. B. *J. Electrochem. Soc.* **1982**, *129*, 2169.

(27) Gardner, R. F. G.; Tanner, D. W.; Sweett, F. *J. Phys. Chem. Solids* **1963**, *24*, 1183.

(28) Akl, A. A. *Appl. Surf. Sci.* **2004**, *221*, 319.

(29) Sugimoto, T.; Muramatsu, A.; Sakata, K.; Shindo, D. *J. Colloid Interface Sci.* **1993**, *158*, 420.

(30) Sugimoto, T.; Waki, S.; Itoh, H.; Muramatsu, A. *Colloids Surf., A* **1996**, *109*, 155.

(31) Ozaki, M.; Ookoshi, N.; Matijevic, E. *J. Colloid Interface Sci.* **1990**, *137*, 546.

(32) Sapieszko, R. S.; Matijevic, E. *J. Colloid Interface Sci.* **1980**, *74*, 405.

(33) Uekawa, N.; Kaneko, K. *J. Phys. Chem. B* **1998**, *102*, 8719.

(34) Thierry, D.; Persson, D.; Leygraf, C.; Boucherit, N.; Hugotlegoff, A. *Corros. Sci.* **1991**, *32*, 273.

(35) Beattie, I. R.; Gilson, T. R. *J. Chem. Soc. A* **1970**, 980.

(36) deFaria, D. L. A.; Silva, S. V.; deOliveira, M. T. *J. Raman Spectrosc.* **1997**, *28*, 873.

(37) Schwertmann, U.; Cornell, R. M. *Iron oxides in laboratory*; VCH: 1991.

(38) Lindgren, T.; Vayssieres, L.; Wang, H.; Lindquist, S. E. Photo oxidation of water at hematite material electrodes. In *Chemical physics of nanostructured semiconductors*; Kokorin, A. I., Bahnemann, D. W., Eds.; VSP: Utrecht, 2003; p 93.

(39) Horowitz, G. *J. Electroanal. Chem.* **1983**, *159*, 421.

(40) Itoh, K.; Bockris, J. O. *J. Appl. Phys.* **1984**, *56*, 874.

(41) Minks, B. P.; Oskam, G.; Vanmaekelbergh, D.; Kelly, J. J. *J. Electroanal. Chem.* **1989**, *273*, 119.

(42) Minks, B. P.; Wiegel, M.; Kelly, J. J. *Electrochim. Acta* **1991**, *36*, 695.

(43) Bard, A. J.; Bocarsly, A. B.; Fan, F. R. F.; Walton, E. G.; Wrighton, M. S. *J. Am. Chem. Soc.* **1980**, *102*, 3671.

(44) Sanchez, H. L.; Steinfink, H.; White, H. S. *J. Solid State Chem.* **1982**, *41*, 90.

(45) Hagfeldt, A.; Bjorksten, U.; Gratzel, M. *J. Phys. Chem.* **1996**, *100*, 8045.

(46) Shinar, R.; Kennedy, J. H. *J. Electrochem. Soc.* **1983**, *130*, 392.